INTERNATIONAL JOURNAL FOR NUMERICAL METHODS IN FLUIDS, VOL. 19, 41–65 (1994)

NEWTON'S METHOD FOR SOLVING HEAT TRANSFER, FLUID FLOW AND INTERFACE SHAPES IN A FLOATING MOLTEN ZONE

C. W. LAN

Chemical Engineering Department, National Central University, Chung-Li, Taiwan 32054, R.O.C.

SUMMARY

Newton's method is applied to the finite volume approximation for the steady state heat transfer, fluid flow and unknown interfaces in a floating molten zone. The streamfunction/vorticity and temperature formulation of the Navier–Stokes and energy equations and their associated boundary conditions are written in generalized curvilinear co-ordinates and conservative law form with the Boussinesq approximation. During Newton iteration the ILU(0) preconditioned GMRES matrix solver is applied for solving the linear system, where the sparse Jacobian matrix is estimated by finite differences. Nearly quadratic convergence of the method is observed. Sample calculations are reported for sodium nitrate, a high-Prandtl-number material ($Pr = 9{\cdot}12$). Both natural convection and thermocapillary flow as well as an overall mass balance constraint in the molten zone are considered. The effects of convection and heat input on the flow patterns, zone position and interface shapes are illustrated. After the lens effect due to the molten zone is considered, the calculated flow patterns and interface shapes are compared with the observed ones and are found to be in good agreement.

KEY WORDS Newton's method, Interface, Floating zone, Thermocapillary flow.

1. INTRODUCTION

The modelling of a floating molten zone is complicated by the strong coupling of mixed natural convection and thermocapillary flow, unknown melt/solid interfaces, an unknown ambient/melt free surface and a constraint of overall mass balance. Numerous computational studies have been carried out to investigate the convection in a melt (or fluid) column between two heated discs, either without free surface deformation[1–6] or with free surface deformation.[7–9] The melt/solid interfaces of all the cases are flat and fixed. The models include either a half-zone configuration (where the temperature of one disc is higher than that of the other) or a full-zone configuration (in which the temperature of both discs is kept the same). The full-zone configuration is similar to the so-called floating zone (FZ) crystal growth process, which is one of the most important processes for purifying or growing high-purity crystals. Recently Duranceau and Brown[10] modelled an FZ crystal growth system using a finite element method (FEM) and computed both melt/solid and melt/air interfaces together with the interacting thermocapillary and natural convections. Lan and Kou[11] also solved the same problem by a body-fitted co-ordinate finite difference method in which the interface shapes were calculated through an outer loop of Gauss–Siedel iteration. The effects of rotation and solute segregation were also investigated by them recently.[12–14] There is a major difference between the modelling of FZ crystal growth and that of a floating molten zone. In practice, to ensure FZ crystal growth at

CCC 0271–2091/94/130041–25

Received 10 September 1993
Revised 3 January 1994

a constant diameter, a growth angle constraint is imposed at the melt/air/crystal triple junction.[15] However, for a floating molten zone the zone is formed by zone melting a solid rod so that the mass of the total sample is constant. The modelling of a floating molten zone considering both melt/solid and melt/ambient (or air) interfaces has not been studied so far; in fact, no attention has been paid to studying this system. However, since forming a floating molten zone is the starting step in FZ crystal growth, a stationary molten zone has its own physical significance. In addition, the capillary phenomena and zone stability of a stationary zone with the volume or mass specified could be quite different from those with the contact angle specified.[16]

From the numerical algorithm point of view the numerical methods used in all the above studies, except the FEM approach, were decoupled iteration approaches. In other words, field variables and free surfaces or interfaces were iterated separately. Although these approaches have proven to be versatile and useful for the class of problems considered,[11–14] the decoupled successive approximations can take many iterations to converge, particularly when extreme underrelaxation is required to ensure stability. Very often a convergence error may be introduced owing to an early termination of the iterations. Further, for problems where limit points, multiple solutions (bifurcation) and instabilities to other solution branches are expected, decoupled successive iterations are not optimal. An alternative to the decoupled approaches of the previous studies is global iteration, in which one could simultaneously iterate on all unknown variables, including the field variables and the unknown interface shapes. Successful implementations of Newton's method in the FEM formulation, a global approach, for free boundary problems has already been reported[10,17,18] and this in fact is seen as a further advantage of the FEM. In the FEM/Newton approach the linear equations were solved by a frontal direct matrix solver.[19] However, for the finite difference or finite volume formulation of free boundary problems Newton's method was not used until recently. Dandy and Leal[20] used Newton's method scheme to solve the shape of a gas bubble in a fluid and the flow patterns around it. Quadratic convergence was also observed in their computation. Both direct and iterative matrix solvers were used to solve the linear Newton equations. The Harwell MA32 frontal matrix solver[21] was particularly recommended. However, owing to the large frontal width caused by the use of natural ordering of variables and elliptic-PDE-generated body-fitted co-ordinates, a large memory space was used in their study. In addition, the computational efficiency of the frontal method was limited by the I/O speed.

In all previous reports the Jacobian matrices used in Newton's method were calculated analytically. Forming a Jacobian matrix analytically is usually extremely tedious and error-prone for free boundary problems, even with the help of symbolic manipulation software. In practice, a small error in the Jacobian matrix can normally deteriorate the quadratic convergence of Newton's method. This therefore makes Newton's method much less attractive for the numerical solution of free boundary problems. Furthermore, in many applications an analytical Jacobian may not be available. Therefore a numerical method (e.g. finite differences) to estimate the Jacobian may provide an easier and more versatile approach in the implementation of Newton's method. Automatic differentiation[22] is another option. In the present paper a global Newton scheme, using a numerical Jacobian instead of an analytical one, is applied to the body-fitted co-ordinate finite volume method (BFCFVM) for solving the floating molten zone problem. Heat transfer, fluid flow and the unknown free surface and interfaces are computed simultaneously and the Newton's method scheme still approaches quadratic convergence.

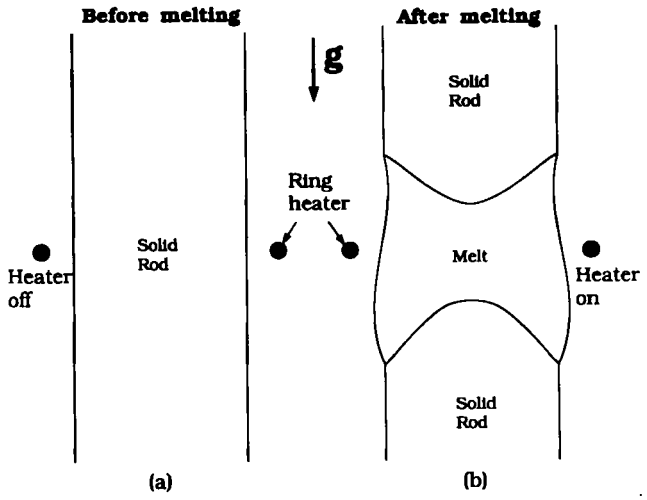

Figure 1. Formation of a floating molten zone from a solid rod: (a) a solid rod before melting; (b) a stationary floating molten zone formed after melting

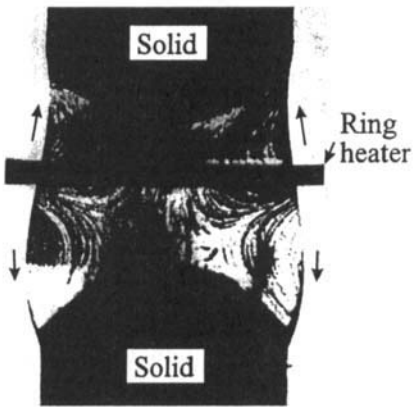

Figure 2. A 2 mm radius $NaNO_3$ floating molten zone in vacuum.[23] The flow patterns were visualized by a 10 mW He–Ne laser. Flow directions are indicated by arrows

2. FORMULATION

2.1. Governing equations

The floating molten zone modelled is illustrated in Figure 1. Figure 1(a) shows the rod material before the heater is switched on. After the heater is turned on for a period of time, a steady state molten zone is obtained as depicted in Figure 1(b). Owing to the effect of gravity, the lower part of the molten zone bulges outwards while the upper part necks inwards. For example, Figure 2 shows the floating molten zone of a 4 mm diameter $NaNO_3$ rod formed by

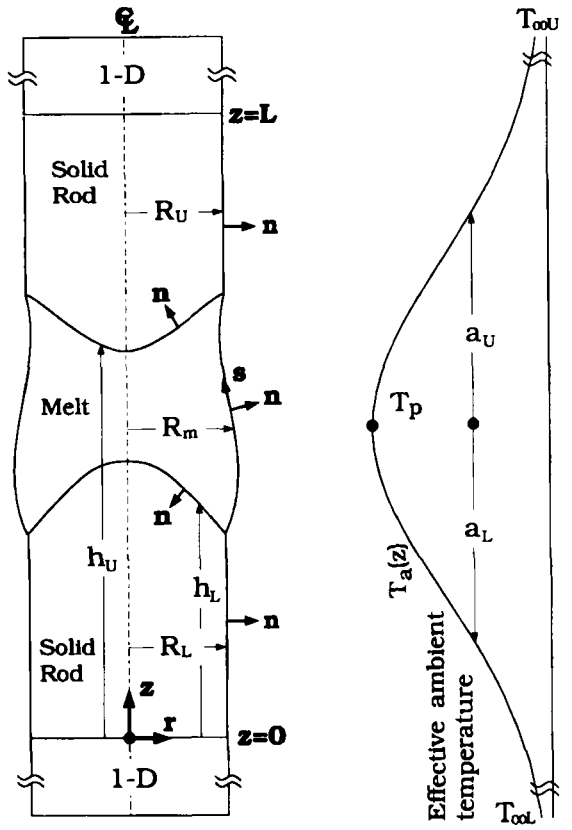

Figure 3. Schematic sketch of a floating molten zone under normal gravity

a platinum heating wire in vacuum.[23] The flow patterns in the melt zone were also visualized by a 10 mW He–Ne laser. As shown, the molten zone not only has a deformed melt/ambient free surface but also highly convex melt/solid interfaces. The directions of flow loops are indicated by the arrows. The flow patterns and their effects on interfaces will be discussed later. Since the modelling of this specific system will be focused on in this paper, the equations described later will be written in dimensional rather than dimensionless forms.

If the heating is axisymmetric, the computational domain for the upper rod, the melt and the lower rod can be taken as shown in Figure 3. Therefore this can be treated as a two-dimensional model. The domain consists of the upper solid rod being held from above, the melt being held by surface tension and the lower solid rod being held from below. Each of these regions is characterized by a set of physical properties. The flow and temperature fields as well as the shapes of the upper solid/melt, lower melt/solid and melt/ambient interfaces are represented in the cylindrical co-ordinate system (r, z).

The total rod length in experiments is usually many times the radius. In order to reduce the computational load, though at the same time compromising the accuracy, the system is divided into three regions. As illustrated in Figure 3, these are an outer region in the upper rod, an outer region in the lower one and an inner region that consists of the melt zone and the solid material near the solid/melt interfaces. The inner region is made long enough so that the

two-dimensional temperature distribution in this region becomes essentially one-dimensional (i.e. uniform in the radial direction) near its two ends. As such, heat transfer in the two outer regions can be treated as one-dimensional. The same strategy has been applied successfully in the numerical simulation of FZ crystal growth.[10,11]

Owing to the unknown boundary shapes, the co-ordinates (r, z) are transformed into general (non-orthogonal) curvilinear co-ordinates (η, ξ) which fit all the interfaces as shown in Figure 4. An algebraic boundary-fitted co-ordinate transformation is used as follows.

Lower rod

$$r = R_L\zeta/[A + (1 - A)\zeta], \tag{1}$$

$$z = h_L[1 - (B_L^{(\xi_a - \xi)} - 1)/(B_L^{(\xi_a - 1)} - 1)], \tag{2}$$

where $\zeta = 0{\cdot}5[\![1 + \tanh\{\delta[(\eta - 1)/(N_x - 1) - 0{\cdot}5]\}/\tanh(0{\cdot}5\delta)]\!]$.

Melt

$$r = R_m\zeta/[A + (1 - A)\zeta], \tag{3}$$

$$z = h_L + (h_U - h_L)\bar{\xi}, \tag{4}$$

where $\bar{\xi} = 0{\cdot}5[\![1 + \tanh\{\delta_m[(\xi - \xi_a)/(\xi_b - \xi_a) - 0{\cdot}5]\}/\tanh(0{\cdot}5\delta_m)]\!]$.

Upper rod

$$r = R_U\zeta/[A + (1 - A)\zeta], \tag{5}$$

$$z = h_U + (L - h_U)(B_U^{(\xi - \xi_b)} - 1)/(B_U^{(\xi_c - \xi_b)} - 1), \tag{6}$$

where A, δ, δ_m, B_L and B_U are the stretch constants to control the grid distributions. The melt/ambient free surface shape $R_m(\xi)$ and the melt/solid interfaces $h_U(\eta)$ and $h_L(\eta)$ are unknown *a priori* and need to be calculated simultaneously with the field variables.

The equations for steady, axisymmetric flows in non-orthogonal co-ordinates using the streamfunction ψ and vorticity ω may be written in a conservative law form as

$$\frac{\partial}{\partial\eta}\left(a\phi\frac{\partial\psi}{\partial\xi}\right) - \frac{\partial}{\partial\xi}\left(a\phi\frac{\partial\psi}{\partial\eta}\right) + \frac{\partial}{\partial\eta}\left[\frac{b}{J}\left(g_{22}\frac{\partial(c\phi)}{\partial\eta} - g_{12}\frac{\partial(c\phi)}{\partial\xi}\right)\right] + \frac{\partial}{\partial\xi}\left[\frac{b}{J}\left(g_{11}\frac{\partial(c\phi)}{\partial\xi} - g_{12}\frac{\partial(c\phi)}{\partial\eta}\right)\right] + Jd = 0, \tag{7}$$

where

$$g_{11} = \left(\frac{\partial r}{\partial\eta}\right)^2 + \left(\frac{\partial z}{\partial\eta}\right)^2, \qquad g_{22} = \left(\frac{\partial r}{\partial\xi}\right)^2 + \left(\frac{\partial z}{\partial\xi}\right)^2,$$

$$g_{12} = \frac{\partial r}{\partial\eta}\frac{\partial r}{\partial\xi} + \frac{\partial z}{\partial\eta}\frac{\partial z}{\partial\xi}, \qquad J = \frac{\partial r}{\partial\eta}\frac{\partial z}{\partial\xi} - \frac{\partial r}{\partial\xi}\frac{\partial z}{\partial\eta}.$$

The coefficients a, b, c and d in equation (7) are given in Table I for $\phi = \psi$, ω and Trespectively. In Table I ρ_L is the melt density, C_p is the specific heat, μ is the viscosity, β is the thermal

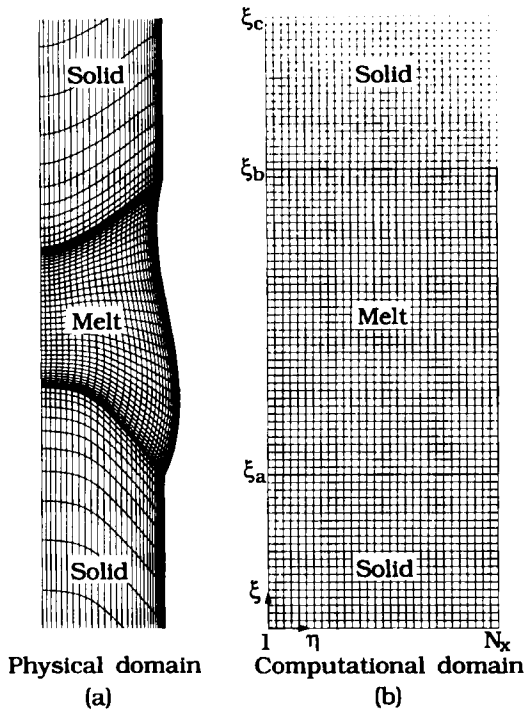

Figure 4. The non-orthogonal body-fitted co-ordinate system used for computation: (a) physical domain; (b) computational domain. The heavy lines are the interfaces in the computational domain

Table I. Coefficients a, b, c and d in equation (7)

ϕ	a	b	c	d
ψ	0	$1/\rho_L r$	1	ω
ω	$1/r$	$1/r$	μr	$-\beta\rho_L g\ \partial T/\partial r$
T	C_p	kr	1	0

expansion coefficient, k is the thermal conductivity and g is the gravitational acceleration. The streamfunction ψ is defined by

$$u = -\frac{1}{\rho_L r}\frac{\partial \psi}{\partial z}, \qquad v = \frac{1}{\rho_L r}\frac{\partial \psi}{\partial r}$$

and the vorticity by

$$\omega = \frac{\partial u}{\partial z} - \frac{\partial v}{\partial r},$$

where u is the radial velocity and v is the axial velocity. Equation (7) can be used in both the melt phase and the solid phase; only the energy equation ($\phi = T$) is needed in the solid phase.

2.2. Boundary conditions

The thermal boundary conditions in the general co-ordinates (η, ξ) are as follows.

(1) Along the centreline of the system ($\eta = 1$), owing to symmetry,

$$g_{22}T_\eta - g_{12}T_\xi = 0. \tag{8}$$

(2) At the melt/solid interfaces ($\xi = \xi_a$, ξ_b) the interfacial energy balance is

$$k\frac{g_{11}T_\xi - g_{12}T_\eta}{Jg_{11}^{1/2}}\bigg|_S - k\frac{g_{11}T_\xi - g_{12}T_\eta}{Jg_{11}^{1/2}}\bigg|_M = 0 \tag{9}$$

and the temperature is set to an equilibrium melting temperature

$$T = T_m, \tag{10}$$

where subscripts S and M denote solid phase and melt phase respectively and T_m is the melting temperature.

(3) At the surface of the solid and melt ($\eta = N_x$), heat transfer from the system to the ambient is by both radiation and convection according to the energy balance along the surface,

$$-k\frac{g_{22}T_\eta - g_{12}T_\xi}{Jg_{22}^{1/2}} = h(T - T_a) + \varepsilon\sigma(T^4 - T_a^4), \tag{11}$$

where $k = k_S$ in the solid and $k = k_M$ in the melt; h is the heat transfer coefficient and is set to zero in vacuum, while ε is the thermal emissivity and σ is the Stefan–Boltzmann constant. $T_a(z)$ is an effective ambient temperature distribution specified along the surface. A Gaussian distribution for $T_a(z)$ as shown in Figure 3 is used.[10–12]

Energy flux continuity is used at the junctions of the one- and two-dimensional regions ($z = 0$ and $z = L$), while an adiabatic condition is employed at the other ends of the one-dimensional regions. The length of the one-dimensional region is about 200 times the rod radius. The implementation of this boundary condition has been described elsewhere.[24]

The fluid flow boundary conditions are as follows.

(1) Along the centreline of the system ($\eta = 1$)

$$\psi = 0, \tag{12}$$

$$\omega = 0. \tag{13}$$

(2) At the melt/solid interfaces ($\xi = \xi_a$, ξ_b)

$$\psi = 0, \tag{14}$$

$$\omega = -\frac{g_{11}}{\rho r J^2}\frac{\partial^2\psi}{\partial\xi^2}. \tag{15}$$

Equation (15) can be derived from the no-slip boundary condition at the solid boundaries, where $u = v = 0$. The streamfunction ψ is set to zero on the boundaries as a reference.

(3) On the free surface of the melt ($\eta = N_x$)

$$\psi = 0, \tag{16}$$

$$\omega = \frac{\partial u}{\partial z} - \frac{\partial v}{\partial r}, \tag{17}$$

with two stress balance equations

$$\mathbf{ns}: \mathbf{t} = \frac{\partial \gamma}{\partial T}(\mathbf{s} \cdot \nabla T), \tag{18}$$

$$\mathbf{nn}: \mathbf{t} = \gamma\left(\frac{1}{R_1} + \frac{1}{R_2}\right) + P_a, \tag{19}$$

where **n** and **s** are the unit normal vector and unit tangent vector at the free surface respectively, **t** is the total stress tensor, γ is the surface tension coefficient of the melt, $\partial\gamma/\partial T$ is the surface tension temperature coefficient of the melt and R_1 and R_2 are the radii of curvature. P_a is a relative reference pressure and is set to satisfy the overall mass balance constraint (which will be described shortly). Along the free surface ψ is zero and $\partial\psi/\partial\xi = 0$. From this it can be shown that $\mathbf{n} \cdot (u\mathbf{e}_r + v\mathbf{e}_z) = 0$. This equation is the so-called kinematic condition.

The tangential stress balance, equation (18), after some manipulation, can be reduced to

$$\omega = -\frac{1}{\mu g_{22}^{1/2}} \frac{\partial \gamma}{\partial T} \frac{\partial T}{\partial \xi} + \frac{2}{g_{22}}\left(\frac{\partial z}{\partial \xi}\frac{\partial u}{\partial \xi} - \frac{\partial r}{\partial \xi}\frac{\partial v}{\partial \xi}\right). \tag{20}$$

Similarly, manipulation of the normal stress balance, equation (19), yields the form

$$\frac{\partial z}{\partial \xi}\frac{\mathrm{d}^2 R_m}{\mathrm{d}\xi^2} - \frac{\partial^2 z}{\partial \xi^2}\frac{\mathrm{d}R_m}{\mathrm{d}\xi} - \frac{g_{22}}{R_m}\frac{\partial z}{\partial \xi} - \frac{S}{\gamma} g_{22}^{3/2} = 0, \tag{21}$$

where S is the total normal stress including the relative pressure difference P_a, the static pressure due to gravity and the dynamic pressure due to fluid flow.[11]

Finally, the overall mass for the sample rod is constant before and after melting, so that this constraint can be conceptually associated with the integration constant, i.e. the relative pressure difference P_a. In fact, in the global iteration scheme described here, P_a is simply treated as one of the unknowns, which is to be determined simultaneously with all other unknowns. The integral equation imposed is

$$\rho_S \pi R_L^2 L - [\rho_S(V_{SU} + V_{SL}) + \rho_L V_M] = 0, \tag{22}$$

where V_{SU} and V_{SL} are the volumes of the upper and lower solid rods respectively, ρ_S is the solid density and V_M is the melt volume. The volume of the lower solid rod can be calculated as

$$V_{SL} = 2\pi \int_1^{\xi_a} \int_1^{N_x} rJ \, \mathrm{d}\eta \, \mathrm{d}\xi \tag{23}$$

and that of the upper one as

$$V_{SU} = 2\pi \int_{\xi_b}^{\xi_c} \int_1^{N_x} rJ \, \mathrm{d}\eta \, \mathrm{d}\xi, \tag{24}$$

while the volume of the molten zone is

$$V_M = 2\pi \int_{\xi_a}^{\xi_b} \int_1^{N_x} rJ \, \mathrm{d}\eta \, \mathrm{d}\xi. \tag{25}$$

It is interesting to point out that the above volume integrals can be evaluated by simple line integrations along the boundaries after co-ordinate transformation; each double integral can be

decomposed into two line integrals. This is another advantage of using algebraically generated body-fitted co-ordinates.

3. FINITE VOLUME DISCRETIZATION

3.1. Finite volume integration

Equation (7) is discretized by employing the finite volume method. The physical domain (r, z) is subdivided into a finite number of control volumes (CVs) of volume V bounded by cell faces, which are located about halfway between consecutive nodal points (see Figure 5). The choice of control volume is quite arbitrary, depending on how the fluxes across cell faces are calculated; different interpolation schemes lead to different 'exact' locations of the cell faces. The physical domain (r, z) can be transformed into the computational domain (η, ξ) according to equations (1)–(6). The transformed domain has a CV of volume V', as shown in Figure 5(b), and $r\mathrm{d}V = rJ\mathrm{d}V'$. Since $\Delta\eta = \Delta\xi = 1$ is used here, $V' = 1$. Also, the cell faces in the domain (η, ξ) are located halfway between nodal points; all variables are stored at the nodal points. For integrating the governing differential equation over the finite control volumes, the Gauss theorem is used. With this the volume integrals of the terms in equation (7) may be converted to surface integrals (fluxes) over the faces of the control volume. The resulting balance equation for each control volume can be expressed as

$$I_e - I_w + I_n - I_s + \int_{V'} (\mathrm{d}J)\, \mathrm{d}\eta\, \mathrm{d}\xi = 0, \tag{26}$$

where I_e, for example, represents the total flux of ϕ across the face 'e'. Each of the surface fluxes I_e, I_w, etc. is made up of two distinct parts, namely a convective contribution I^C and a diffusive contribution I^D. Equation (26) represents the finite volume equation of the differential

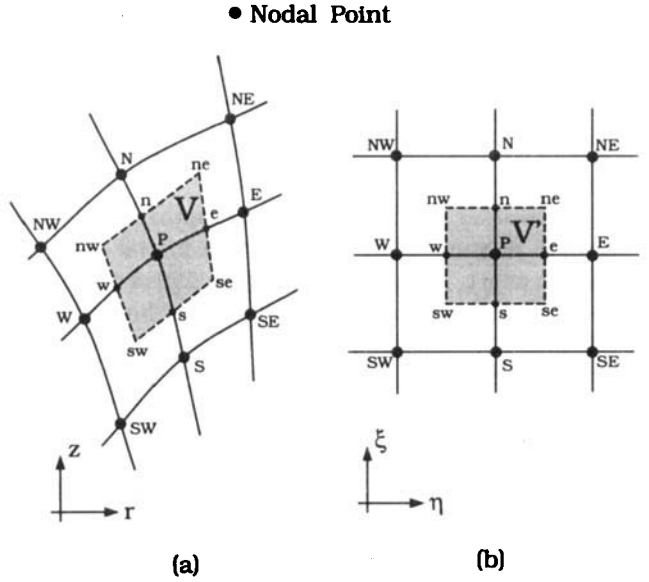

Figure 5. Nodal points and finite volume in (a) the physical domain and (b) the computational domain

equation governing ϕ. The numerical evaluation of the various terms in equation (26) requires the calculation of geometrical factors for control volumes and a discretization scheme for interpolating quantities at the cell faces from their nodal values.

The above treatment is similar to that of Lan and Kou.[25] The major difference is that a conservative law (divergence) form of the governing equation (7) is used here instead of a non-conservative one. Mathematically these two formulations are exactly the same and can be transformed into each other simply by the chain rule, but numerically they are not. By the present approach the flux balance within the finite volume is conservative. In other words, equation (26) guarantees that the internal fluxes will be cancelled when it is summed over all the control volumes. On the other hand, in the non-conservative formulation fictitious sources due to the finite difference approximation may be introduced during the summation procedure. Hence, a better conservation of field properties is expected using the conservative form.

3.2. Evaluation of convection, diffusion and source terms

Linear interpolation is used to calculate the values of ϕ and the co-ordinate values (r, z) at the cell faces for evaluating the diffusive flux I^D. Values at the corners of the control volume are obtained by taking average values over their nearby nodal points. For the convective fluxes I^C at the cell faces an upwind scheme[26] is adopted. Accordingly the expression for the convective flux of ϕ through the cell face 'e', for example, can be written as

$$I_e^C = (a\phi)_e(\psi_{ne} - \psi_{se}), \tag{27}$$

where

$$a\phi_e = 0{\cdot}5(a\psi)_P[(\psi_{ne} - \psi_{se}) - |\psi_{ne} - \psi_{se}|] + 0{\cdot}5(a\psi)_E[(\psi_{ne} - \psi_{se}) + |\psi_{ne} - \psi_{se}|], \tag{28}$$

the diffusive flux as

$$I_e^D = \left(\frac{bg_{22}}{J}\right)_e [(c\phi)_E - (c\phi)_P] - \left(\frac{bg_{12}}{J}\right)_e [(c\phi)_{ne} - (c\phi)_{se}], \tag{29}$$

and the source term as

$$\int_{V'} (\mathrm{d}J)\, \mathrm{d}\eta\, \mathrm{d}\xi = (\mathrm{d}J)_P. \tag{30}$$

The reasons for using the first-order upwind scheme to approximate the convective terms are firstly to ensure the diagonal dominance of the Jacobian matrix for numerical stability and secondly to reduce the coding effort. The central difference scheme, even though it has a higher order of accuracy, could lead to slow convergence or instability during linear equation iterations. Second-order upwind schemes not only require more coding effort but also lead to a larger bandwidth in the Jacobian matrix.

3.3. Boundary conditions

Apparently the control volumes on the boundaries are all half-cells. With the ψ/ω formulation, integrating the governing equations over the half-cells with the import of the boundary conditions requires more coding effort for free boundary problems. Instead, second-order finite difference approximations of the boundary conditions are used directly here; the one-side difference is employed in the normal direction and the central difference is employed

in the other direction. It has been noted that an inconsistent treatment of the finite volume method on the boundaries may affect the accuracy.[27] However, through a series of mesh refinements it was found that the hybrid approach gave satisfactory results even for the coarsest mesh used in the study.

Simpson's rule is used for volume integration, i.e. equations (23)–(25), while the trapezoidal rule is used for integration of the pressure along the free surface. The reason for using the two different schemes is that although Simpson's rule has a higher accuracy than the trapezoidal rule, it requires that the number of points in the integration be odd for volume integration, but for integrating the pressure over the free surface (from ξ_a to ξ_b) the number of points alternates between odd and even as the integration proceeds. Because of this, N_x, ξ_a, $\xi_b - \xi_a + 1$ and $\xi_c - \xi_b + 1$ are all odd numbers. The normal stress balance at the free surface, equation (21), is approximated by second-order differences as well.

3.4. Algebraic equations

Equation (26) and the discretization of the boundary conditions yield $\xi_c N_x$ algebraic equations for T(in the two-dimensional domain), $(\xi_b - \xi_a - 1)(N_x - 2)$ equations for ψ and $(\xi_b - \xi_a + 1)N_x$ equations for ω. Discretization of the interface boundary conditions yields $2N_x$ equations for h_U and h_L and $\xi_b - \xi_a + 1$ algebraic equations for R_m. In addition, there are one equation for the relative pressure difference P_a and an additional 60 equations for the temperature in the one-dimensional regions. In total there are therefore $\xi_c N_x + (\xi_b - \xi_a - 1)(N_x - 2) + (\xi_b - \xi_a + 1)N_x + 2N_x + (\xi_b - \xi_a + 1) + 1 + 60$ equations and unknowns. For example, in the case of 31×81 grid points in the domain ($N_x = 31$ and $\xi_c = 81$) there are 5077 equations and unknowns.

4. SOLUTION SCHEME

4.1. Newton's method

The system of non-linear algebraic equations generated in the previous section can be written symbolically as

$$\mathbf{f}(\mathbf{x}) \equiv \mathbf{f}(T, \psi, \omega, R_m, h_U, h_L, P_a) = \mathbf{0}. \tag{31}$$

This non-linear equation set is solved by Newton's method simultaneously for all variables. Starting from an initial approximation $\mathbf{x}^0$ to the vector of unknowns, successive updates are constructed as

$$\mathbf{x}^{n+1} = \mathbf{x}^n + \boldsymbol{\delta}^{n+1}, \tag{32}$$

where the correction vector $\boldsymbol{\delta}^{n+1}$ is the solution of the linear equation set

$$\mathbf{J}\boldsymbol{\delta}^{n+1} = -\mathbf{f}(\mathbf{x}^n). \tag{33}$$

The components of the Jacobian matrix $\mathbf{J}$, formed by explicit differentiations as $J_{ij} \equiv \partial f_i / \partial x_j$, represent the sensitivity of the residual vector to changes in the solution vector.

4.2. Jacobian matrix

To achieve a tight band structure in the Jacobian matrix, the equations and unknowns are ordered, starting at η, $\xi = 1$ for each ξ, in order of appearance. In the lower solid rod N_x

equations are written for T for each ξ. In the melt, starting at $\xi = \xi_a$, N_x equations are written for T, ψ and ω; there are three degrees of freedom per nodal point. In the upper solid rod, starting at $\xi = \xi_b + 1$, the ordering is similar to that in the lower rod. After the governing equation (26) and the associated boundary conditions have been written, the boundary conditions are included in the following order: the lower solid/melt interface energy balance, the upper melt/solid interface energy balance, the normal stress balance and finally the overall mass balance. Because the relative pressure difference P_a does not appear explicitly in the overall mass balance equation, the last diagonal element of the Jacobian matrix is zero. The sparse structure arising from this ordering is shown in Figure 6; the sparsity is only about 0.6%. The vertical band on the right shows the dependence of the field variables on the interfaces. For high-Prandtl-number materials the interface shapes are strongly affected by T, ψ and ω. The omission of some elements in this vertical band will cause slow convergence or divergence during Newton iteration. In fact, the 'arrow-shaped' structure, similar to that from the FEM approximation,[17,18] is typical in free boundary or interface problems.

A Jacobian matrix with a known sparse pattern could be estimated either analytically or numerically. Getting an analytical Jacobian for a large and complicated problem is usually difficult and error-prone, even with the help of symbolic differentiation, especially as the complexity increases. The finite difference approach proves to be an efficient way to compute the derivatives and has the advantage that one needs only the residual function $\mathbf{f}(\mathbf{x})$ as a 'black box'. For a residual vector $\mathbf{f}(\mathbf{x})$ with dimension NEQ (the total number of equations) the simplest way to approximate $\tilde{\mathbf{J}}$ is to use forward differences

$$\frac{\partial f_i}{\partial x_j} \approx \frac{f_i(\mathbf{x} + h_j \mathbf{e}_j) - f_i(\mathbf{x})}{h_j}, \tag{34}$$

where $\mathbf{e}_j$ is column j of the identity matrix and h_j is a suitable step length. A straightforward implementation of equation (34) requires computing $\mathbf{f}(\mathbf{x} + h_j \mathbf{e}_j)$ for each j, i.e. NEQ evaluations

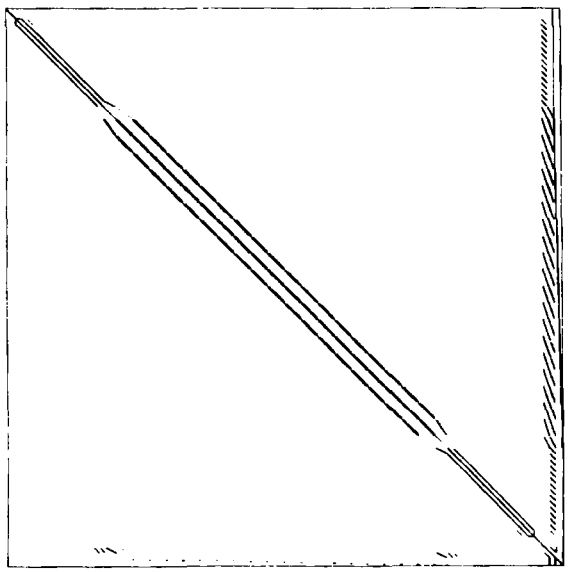

Figure 6. Sparse structure of the Jacobian matrix

of $\mathbf{f}$ at displacements from $\mathbf{x}$. However, because of the sparsity, each f_i depends only on a few x_j. Therefore one can use this fact to reduce the number of function evaluations.

For a sparse matrix with any pattern Curtis *et al.*[28] proposed a heuristic, the so-called CPR algorithm, to group columns of $\tilde{\mathbf{J}}$ such that no two have entries in the same row. A set of such columns of $\tilde{\mathbf{J}}$ can be computed simultaneously with a single residual function evaluation. To further improve the algorithm, Coleman *et al.*[29] proposed an *a priori* permutation of columns to alter the order in which they are examined or to apply the algorithm to $\tilde{\mathbf{J}}^{\mathrm{T}}$ rather than $\tilde{\mathbf{J}}$. Sometimes such an approach reduces the number of groups slightly. Software for their new algorithm, although the improvement to the CPR algorithm is minor, is adopted here to estimate the Jacobian matrix with the least possible number of function evaluations. The number of function evaluations is about 104 for $NEQ = 5077$ and about 40 if the overall mass balance constraint (the last equation) is excluded. In fact, the Jacobian elements for the mass integral equation could be easily evaluated analytically and this reduces by more than half the computational effort on the residual function. It should be pointed out that the minimum number of function evaluations is equal to the number of equations if there exists any row that is full.[30]

After the groups of columns are found, equation (34) is then used to compute the elements of $\tilde{\mathbf{J}}$. However, a small step size (h_j) is needed to properly approximate derivatives, yet it may lead to numerical cancellation and the loss of many digits of accuracy. In addition, different scales of x_j may require different step sizes for the various independent variables. The step size for x_j is estimated by

$$h_j = \sqrt{\epsilon}\,\max(|x_j|,\ RTOL_j|x_j| + ATOL_j), \tag{35}$$

where $RTOL_j$ and $ATOL_j$ are the relative and absolute error tolerances specified respectively and ϵ is the unit round-off error of the computer. For most variables $RTOL$ and $ATOL$ are of the order of 1×10^{-3}, except for the vorticity. For the vorticity a larger $ATOL$ is needed to ensure stability. In most cases $ATOL \approx 1$ is adequate for the vorticity; a larger value may be helpful for cases with stronger convection. Too large a value of h_j could slow down the convergence speed as well.

4.3. Solution of linear equations

Solving the linear equation (33) requires a sparse matrix package that efficiently stores the elements of the Jacobian and also provides a fast and accurate solution. A direct matrix solver, i.e. Harwell MA28,[31] and two iterative matrix solvers, i.e. GMRES[32] and CGS[33] with incomplete LU factorization without fill-in, ILU(0), are examined. Among these, CGS fails to converge and MA28 costs too much memory and computation time. For MA28 especially a threshold value of at least 0.1 for partial pivoting is required to ensure stability, which leads to too many fill-in elements and too much CPU time in the analysis phase (where the sparse pattern is analysed to find an ordering that preserves sparsity) during LU factorization. Only GMRES performed well in this study from the consideration of CPU time, memory and robustness.

GMRES is a technique introduced by Saad and Schultz[32] for solving a large sparse non-symmetric linear system of equations by minimizing the 2-norm (Euclidean norm) of the residual vector $-\mathbf{f} - \tilde{\mathbf{J}}\boldsymbol{\delta}$ over $\boldsymbol{\delta}$ in the Krylov subspace

$$\mathbf{K}_m = \mathrm{Span}\{\mathbf{r}_0, \tilde{\mathbf{J}}\mathbf{r}_0, \ldots, \tilde{\mathbf{J}}^{m-1}\mathbf{r}_0\}, \tag{36}$$

where $\mathbf{r}_0$ is the initial residual vector $-\mathbf{f} - \tilde{\mathbf{J}}\boldsymbol{\delta}_0$ and m is the dimension of the Krylov space. Preconditioning plays a very important role in the application of an iterative matrix solver. The

idea of preconditioning is simply to transform the original linear equation set, e.g. by multiplying it through by a certain matrix $\mathbf{P}^{-1}$, into one that can be easier to solve by a Krylov subspace method. For example, when the preconditioner $\mathbf{P}$ is applied to the right of the matrix, one will be solving, instead of equation (33), the preconditioned linear system

$$(\tilde{\mathbf{J}}\mathbf{P}^{-1})(\mathbf{P}\boldsymbol{\delta}) = -\mathbf{f}. \tag{37}$$

The incomplete LU decomposition without fill-in, ILU(0),[34] is one of the simplest and most popular preconditioners. The principle is to find a pair of matrices L and U, where L is a unit lower triangular and U an upper triangular matrix, such that $L + U$ has the same structure as the original matrix and $(LU)_{ij} = \tilde{J}_{ij}$ for each pair (i, j) that belongs to the non-zero structure of $\tilde{J}$. The most common way to obtain ILU(0) is to perform standard Gaussian elimination and during the process replace any fill-in by zero. Clearly the zeros that are introduced need not be stored. Since ILU(0) does not perform pivoting during factorization, it may fail owing to the zero diagonal elements in the Jacobian matrix. Therefore a proper ordering of the variables is crucial to the success of iterative matrix solvers. Furthermore, increasing the dimension m of $\mathbf{K}_m$ could reduce the number of iterations to convergence, but the memory space required is increased as well. A value of $m = 75$ is used in the calculations. In such a case GMRES takes about 80 iterations to converge with a 2-norm of 10^{-6}.

4.4. Verification of numerical scheme

The numerical solutions can be affected by three kinds of errors:[35] (1) algorithmic and coding errors, (2) convergence error (error due to the difference between the exact solution and the approximate solution of the discretized equations left over after stopping the iterations) and (3) discretization error (due to the difference between exact and numerical solutions). In order to examine the first type of error, the results of the present code are compared with those from a finite element code developed by Hyer *et al.*[8] as well as with the velocity distribution measurements by Preisser *et al.*[36] for the half-zone configuration and are found to be in good agreement. A detailed discussion of the comparison is given elsewhere.[9] The second type of error is the most common one in free boundary problems using the successive approximation (decoupled) approach. In many problems the convergence rate of free surfaces could be very slow when compared with other variables. The method of updating free surface shapes can also affect the convergence speed significantly.[37] Stopping the iterations too early is very likely to introduce this type of error. Fortunately, the error could be minimized easily by setting strict convergence criteria. In this study an infinity norm of 1×10^{-6} is used for both residual and correction vectors as the stopping criterion for Newton iterations. To examine the third type of error, mesh refinement is performed. Results obtained by three different meshes are compared and will be illustrated in Section 5.

This study is mainly motivated by experimental observations (e.g. Figure 2) of a stationary, 2 mm radius, $NaNO_3$ floating molten zone in vacuum.[23] Therefore the numerical scheme developed here is aimed to study this specific system. The physical properties of $NaNO_3$ listed in Table II are used in this study unless otherwise stated. According to the table, sodium nitrate ($NaNO_3$) is a high-Prandtl-number material ($Pr = 9.12$) and has a high surface tension temperature coefficient ($\partial\gamma/\partial T = -0{\cdot}056$ dyn cm^{-1} K^{-1}) as well as a high thermal expansion coefficient ($\beta = 6{\cdot}6 \times 10^{-4}$ K^{-1}). Therefore it is an excellent candidate for studying the interaction of thermocapillary flow and natural convection and the effects on interface shapes. In fact, $NaNO_3$ has been used to study floating molten zones or FZ crystal growth by many authors[36,38,39] and its physical properties are well documented.[36] In the following section the effects of natural

Table II. Physical properties of $NaNO_3$[12]

$T_m = 306{\cdot}8\ ^\circ C$
$\Delta H = 182\ J\ g^{-1}$
$h = 0\ W\ cm^{-2}\ ^\circ C^{-1}$
$k_S = 5{\cdot}65 \times 10^{-3} + 33{\cdot}5(T - 230) \times 10^{-7}\ W\ cm^{-1}\ ^\circ C^{-1}$
$k_M = 5{\cdot}65 \times 10^{-3} + 44{\cdot}7(T - T_m) \times 10^{-7}\ W\ cm^{-1}\ ^\circ C^{-1}$
$C_{p_S} = C_{p_L} = 1{\cdot}255 + 2{\cdot}18(T - 100) \times 10^{-3}\ J\ g^{-1}\ ^\circ C^{-1}$
$\partial\gamma/\partial T = -0{\cdot}056\ dyn\ cm^{-1}\ ^\circ C^{-1}$
$\gamma = 119{\cdot}96 + (T - T_m)\ \partial\gamma/\partial T\ dyn\ cm^{-1}$
$\mu = 0{\cdot}0302 - 1{\cdot}533 \times 10^{-4}(T - T_m)\ g\ cm^{-1}\ s^{-1}$
$\beta = 6{\cdot}6 \times 10^{-4}\ ^\circ C^{-1}$
$\varepsilon_S = 0{\cdot}7$
$\varepsilon_L = 0{\cdot}7$
$\rho_S = 2{\cdot}118\ g\ cm^{-3}$
$\rho_L = 1{\cdot}904\ g\ cm^{-3}$

convection on heat flow and interface shapes are discussed first, then the effects of thermocapillary flow. Furthermore, a sample comparison of calculated results with the observed ones from Figure 2 is illustrated. Finally, the effect of heat input is demonstrated, followed by a brief conclusion in Section 6.

5. RESULTS AND DISCUSSION

5.1. Natural convection

Owing to the high Prandtl number of $NaNO_3$, the effect of convection on heat transfer could be very significant in the molten zone. Therefore the numerical results for $NaNO_3$ may be vulnerable to the grid systems used in the computation. Before the effect of buoyancy-induced flow (natural convection) is discussed, the effect of the discretization on the accuracy of the calculations is examined through a sequence of calculations for $\beta = 6{\cdot}6 \times 10^{-4}\ K^{-1}$ (a real value) and $\partial\gamma/\partial T = 0$. Figure 7 shows three different meshes used for a 2 mm radius rod of $NaNO_3$ with a length of 10 cm in the two-dimensional region ($L = 10$ cm). The grids, given in the order of upper rod, melt and lower rod for each case, are 21 × 21, 21 × 31 and 21 × 21 in Figure 7(a), 31 × 21, 31 × 41 and 31 × 21 in Figure 7(b) and 41 × 21, 41 × 51 and 41 × 21 in Figure 7(c). The total numbers of unknowns are 2827, 5077 and 7927 respectively. The effective ambient temperature distribution is also shown on the LHS of Figure 7, in which $T_p = 540\ ^\circ$, $T_{a\infty} = 25\ ^\circ C$ and $a_U = a_L = 0{\cdot}3$ cm. The calculated results based on the grids in Figures 7(a)–7(c) are shown in Figures 8(a)–8(c) respectively. In each figure the LHS shows the streamline and the RHS the isotherms. The arrows indicate the direction of flow. The streamlines are equally spaced at $\Delta\psi = \psi_{max}/10$ for the positive ones and at $\Delta\psi = \psi_{min}/10$ for the negative ones. The isotherms are also equally spaced at $\Delta T_{melt} = (T_{max} - T_m)/10$ in the melt and $\Delta T_{solid} = 8\Delta T_{melt}$ in the solid. These definitions of $\Delta\psi$ and ΔTwill be used throughout this study. The calculated results based on the meshes shown in Figures 7(b) and 7(c) are significantly closer to each other; in fact, all of them are very close to one another. In order to have a reasonable balance between accuracy and CPU time, meshes similar to that in Figure 7(b) are used for all the calculations in this paper. Furthermore, as can be noted in Figure 7, the grid spacing is finer near the interfaces and free surfaces. This is to enhance the accuracy of the finite volume approximation

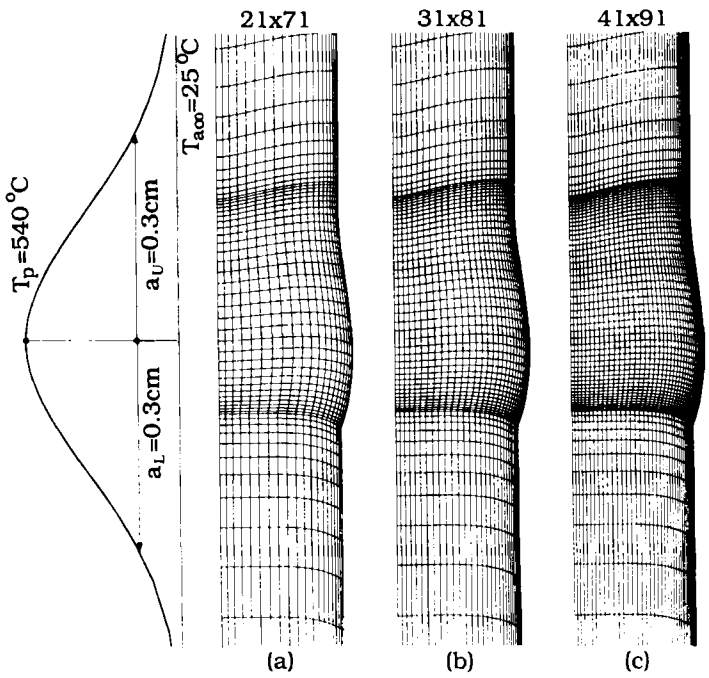

Figure 7. Three different grids used for a floating molten zone with natural convection: (a) 21 × 21 (lower rod), 21 × 31 (melt zone), 21 × 21 (upper rod); (b) 31 × 21, 31 × 41, 31 × 21; (c) 41 × 21, 41 × 51, 41 × 21. The effective ambient temperature distribution is shown on the LHS

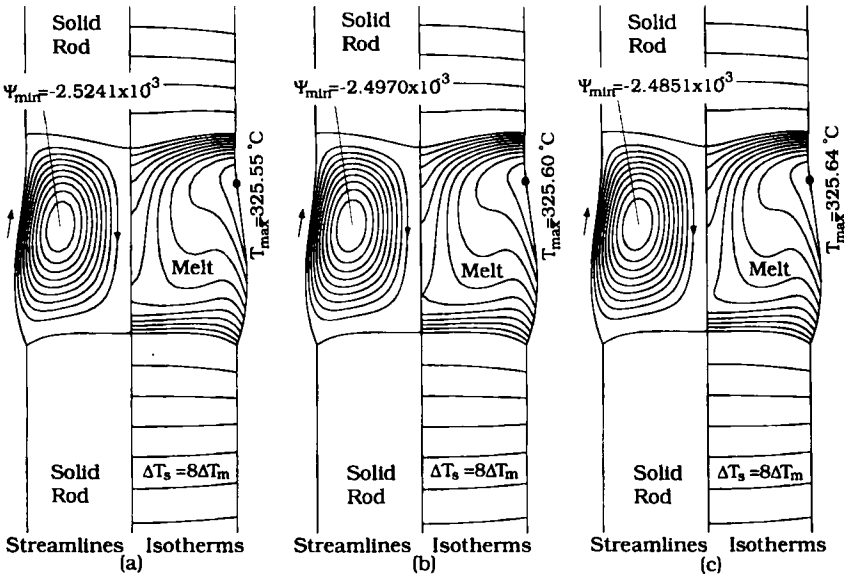

Figure 8. Calculated results based on the grids in (a) Figure 7(a), (b) Figure 7(b) and (c) Figure 7(c). The LHS shows the streamlines and the RHS the isotherms. $\Delta\psi = \psi_{max}/10$ for positive ψ, $\Delta\psi = \psi_{min}/10$ for negative ψ, $\Delta T_m = (T_{max} - T_m)/10$ and $\Delta T_s = 8\Delta T_m$

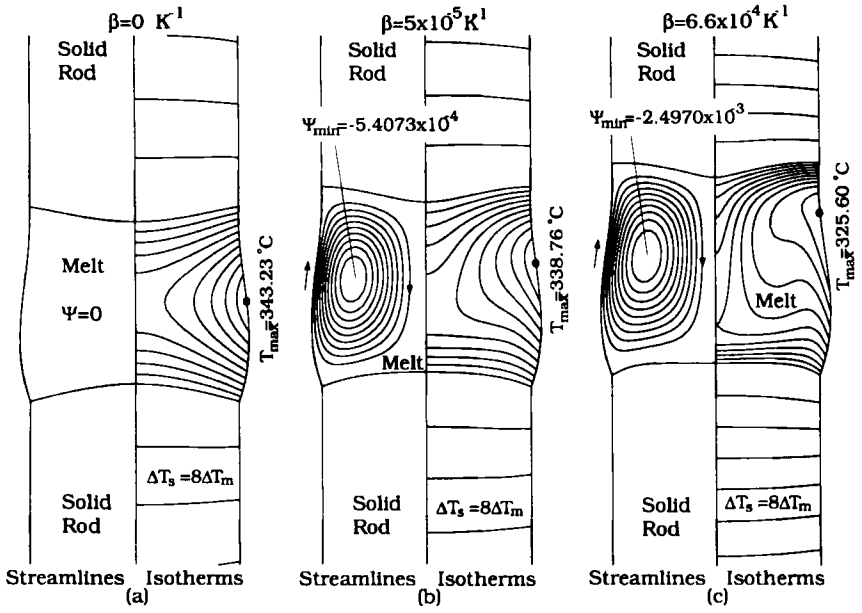

Figure 9. Effect of natural convection: (a) $\beta = 0\ K^{-1}$, (b) $\beta = 5 \times 10^{-5}\ K^{-1}$; (c) $\beta = 6{\cdot}6 \times 10^{-4}\ K^{-1}$

to the higher velocity and temperature gradients there. The stretch constants for the grid distribution are $A = 0.4472$, $\delta = 2.4224$, $B_L = B_U = 1.3$ and $\delta_m = 3.0$. Similar mesh placements have been used in the simulation of FZ crystal growth.[11–14]

The effects of natural convection are demonstrated through three different sets of β. The calculated results are shown in Figure 9. The case of $\beta = 0$ and $\partial\gamma/\partial T = 0$, i.e. conductive heat transfer only, is shown in Figure 9(a). As can be seen, the streamline is zero everywhere, which means no convection in the molten zone. Owing to gravity, the lower part of the molten zone bulges outwards. Since the density of solid ($\rho_S = 2.1173\ g\ cm^{-3}$) is larger than that of the melt ($\rho = 1.903\ g\ cm^{-3}$), the total volume increases after melting. As such, unlike the previous reports[7–9] where the melt and solid densities were assumed to be the same, the upper part of the molten zone does not neck inwards at this zone length. The melt/solid interfaces are slightly convex towards the melt. The maximum surface temperature is 343·23 °C, which represents a rather high superheating (36·43 °C).

When β is increased to $5 \times 10^{-5}\ K^{-1}$, natural convection is induced. As shown in Figure 9(b), there is one flow loop in the melt and it is clockwise in direction. The hotter and lighter melt near the free surface floats upwards, while the cooler and heavier melt near the centreline sinks, thus producing a flow loop. Owing to the action of the flow loop, heat transfer to the upper melt/solid interface is encouraged, while that to the lower melt/solid interface is discouraged. Consequently, the overall position of the melt zone and the location of the maximum temperature shift upwards as compared with those in Figure 9(a). However, the melt/solid interfaces are still very flat. When β is further increased to $6{\cdot}6 \times 10^{-4}\ K^{-1}$, these effects become more significant. Not only do the zone position and the T_{max} location shift upwards more, but the isotherms also become highly distorted; the zone length is increased as well owing to the stronger convective heat transfer. At this β value $T_{max} = 325{\cdot}60$ °C, which represents a 17·65 °C decrease due to natural convection as compared with that of conduction alone ($T_{max} = 343{\cdot}23$ °C).

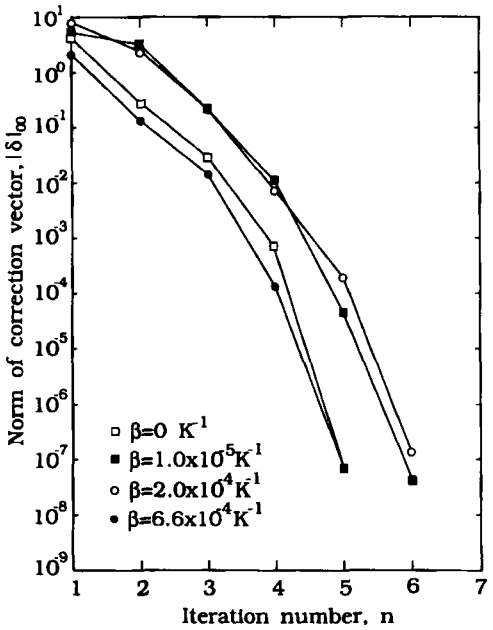

Figure 10. Convergence of Newton iteration scheme for various values of β

The robustness of the simultaneous Newton iteration for the field variables and interface shapes is evident in Figure 10 by the convergence (measured by the infinity norm of δ) with the number of Newton iterations for computations with various β. Initial guesses for each calculation are provided quite arbitrarily, either by a linear temperature distribution without convection ($\beta = 0$) or by using the converged solution with a smaller value of β. In each calculation the iterations converge nearly quadratically after two or three iterations.

5.2. Thermocapillary flow

Since the free surface of the molten zone is not isothermal, the surface tension gradient due to the temperature difference could induce fluid flow, the so-called thermocapillary convection. Different levels of thermocapillary convection can be introduced by setting different values of $\partial\gamma/\partial T$ and these are presented in Figure 11; Figure 11(a) is taken from Figure 10(c) for comparison. When $|\partial\gamma/\partial T|$ is increased to $8{\cdot}624 \times 10^{-3}$ dyn cm^{-1} K^{-1}, as shown in Figure 11(b), near the free surface a small flow loop in the lower part of the molten zone is induced and the flow direction is counterclockwise. Since $\partial\gamma/\partial T$ is negative, the surface flow is towards the melt/solid interfaces where the surface tension is the highest. As a result, the flow delivers heat to the melt/solid interfaces and thus results in a melting back at the solid/melt interfaces near the free surface. The intensity of the upper flow loop is also enhanced, since the thermocapillary flow and natural convection are in the same direction, i.e. clockwise. Clearly, as compared with Figure 11(a), the intensity of the upper loop in Figure 11(b), $\psi_{min} = -2{\cdot}7166 \times 10^{-3}$ g s^{-1}, becomes stronger and the flow loop penetrates more into the corner near the free surface; the asterisk indicates the zero streamline. Hence heat transfer is encouraged to the upper melt/solid interface but is discouraged near the centreline. As a result, the melt

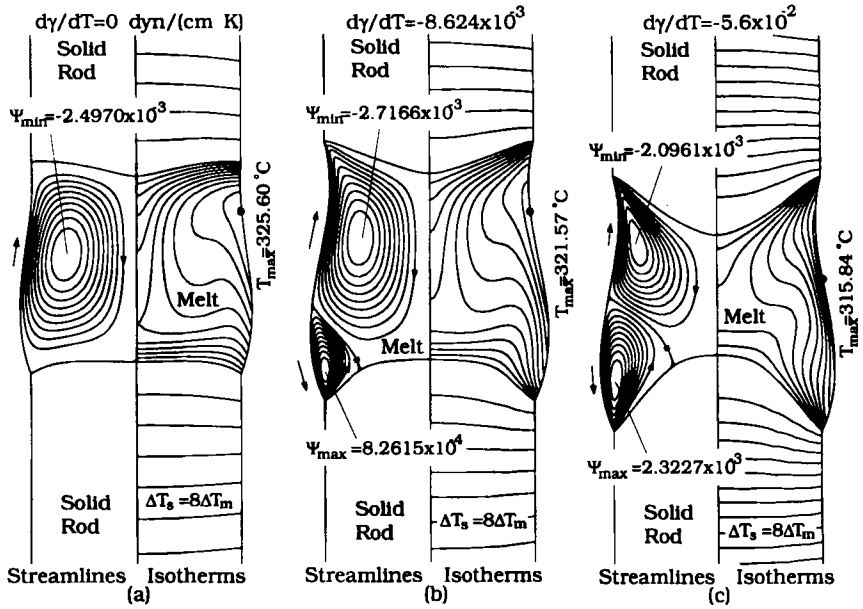

Figure 11. Effect of thermocapillary flow: (a) $\partial\gamma/\partial T = 0$ dyn K^{-1} cm^{-1}; (b) $\partial\gamma/\partial T = -8{\cdot}624 \times 10^{-3}$ dyn K^{-1} cm^{-1}; (c) $\partial\gamma/\partial T = -0{\cdot}056$ dyn K^{-1} cm^{-1}. $\beta = 6{\cdot}6 \times 10^{-4}$ K^{-1} in all cases

zone is significantly longer at the free surface and slightly shorter at the centreline and the free surface deformation increases as compared with Figure 11(a). When $|\partial\gamma/\partial T|$ is further increased to 0·056 dyn cm^{-1} K^{-1}, the lower convection loop increases and melts back the lower melt/solid interface even more. Surprisingly, the intensity of the upper loop decreases, while the position of the zone and T_{max} shift downwards. The zone length decreases only slightly at the free surface but decreases significantly at the centreline. Meanwhile, the melt/solid interfaces become significantly more convex, which is consistent with those observed in experiments (Figure 2). Obviously the thermocapillary flow is pervasive in the molten zone. In fact, these phenomena can only be observed through a floating molten zone model with the consideration of unknown melt/solid interfaces. Indeed, when an effective ambient temperature is given, the heat input can be affected not only by the zone shape but also by the zone position relative to the heater. Therefore the floating zone model proposed by Zhang and Alexander,[7] where the melt/solid interfaces are flat and fixed, is inadequate to describe a floating molten zone.

Since the thermocapillary convection prevails over the buoyancy-driven one, the grid system used needs to be examined once more to ensure the validity of the results. The three different meshes shown in Figure 12, similar to the ones in Figure 7, are tested and the results based on these grids are illustrated in Figure 13. As can be seen, all the results are very close to one another. From Figures 13(a)–13(c) they all converge within seven Newton iterations and each Newton iteration takes 15, 33 and 50 s CPU time respectively on an HP735 workstation.

5.3. Comparison with experimental observation

In this subsection the calculated results are compared with the experimental ones shown in Figure 2. If Figure 2 is examined closely, it is found out that the zone length of the lower part of the molten zone, with respect to the ring heater, is longer than that of the upper part.

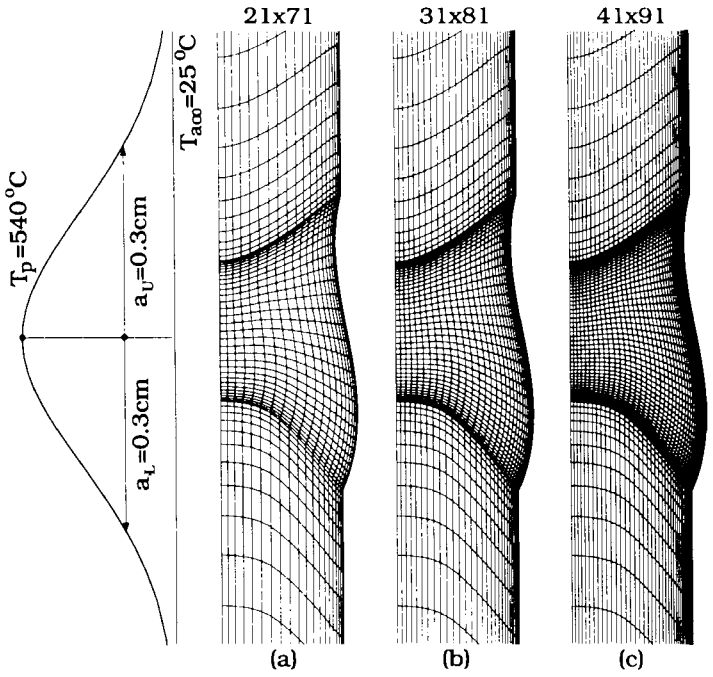

Figure 12. Three different grids used for a floating molten zone with natural convection and thermocapillary flow: (a) 21 × 21 (lower rod), 21 × 31 (melt zone), 21 × 21 (upper rod); (b) 31 × 21, 31 × 41, 31 × 21; (c) 41 × 21, 41 × 51, 41 × 21. The effective ambient temperature distribution is shown on the LHS

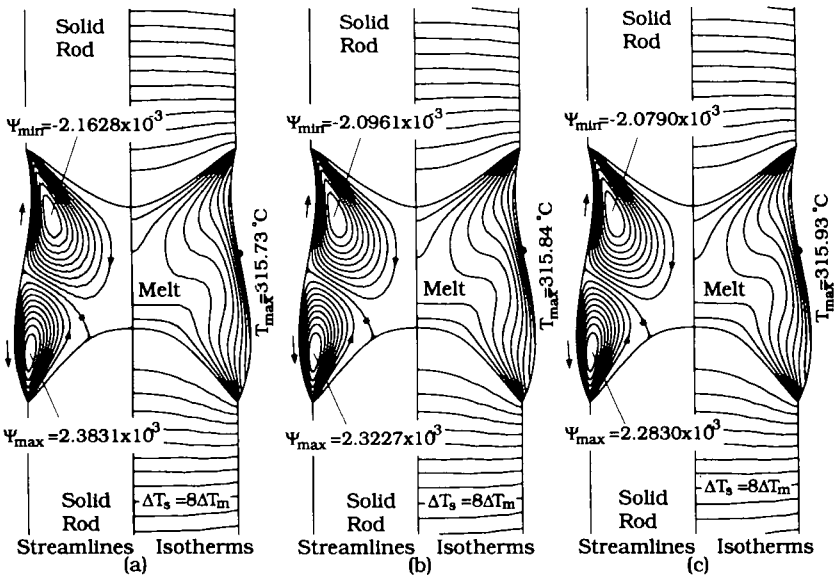

Figure 13. Calculated results based on the grids in (a) Figure 12(a), (b) Figure 12(b) and (c) Figure 12(c). The LHS shows the streamlines and the RHS the isotherms

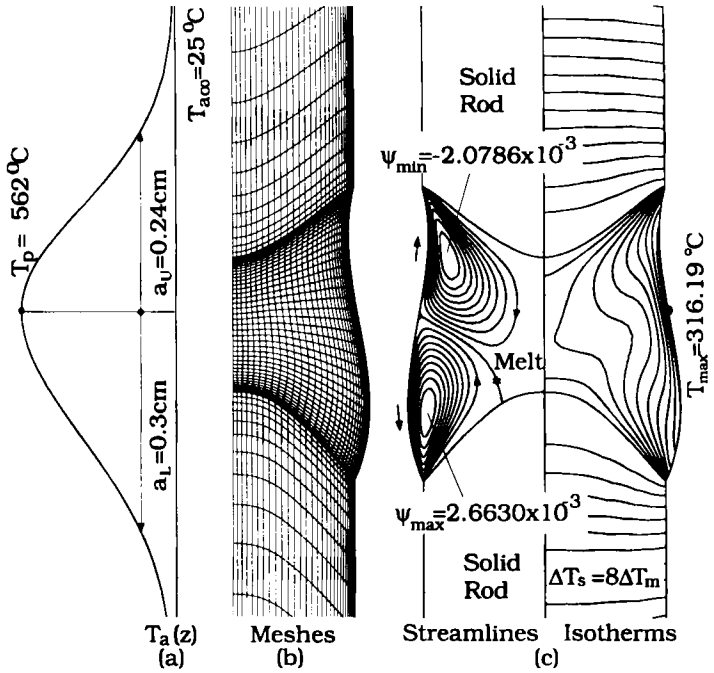

Figure 14. Calculated results for the comparison with Figure 2: (a) effective ambient temperature; (b) mesh system; (c) calculated flow patterns, isotherms and interface shapes

There are two factors that could be directly responsible for this: (1) free surface deformation and (2) thermocapillary flow. In the lower part of the zone the free surface bulges out and makes itself closer to the heater and thus receives more heat. On the other hand, the bulging free surface also provides more space for convection to develop. Thus the convective heat transfer is enhanced and tends to melt back the melt/solid interface more. As seen in Figure 11(c), the second effect is not dominant for the present zone length. Regarding the first factor, the symmetrical effective ambient temperature distribution that has been used so far seems not to be realistic. To improve this, the width parameters a_U and a_L of $T_a(z)$ are assigned to be different. In other words, the symmetrical effective ambient temperature distribution is modified to an asymmetrical one to simulate the effect of view factors. The asymmetrical $T_a(z)$ is shown in Figure 14(a). As can be seen, the deviation of the distribution from the symmetrical one is very small. The mesh and the calculated results based on this $T_a(z)$ are shown in Figures 14(b) and 14(c) respectively. As can be seen, owing to the asymmetrical heating profile, the molten zone shifts downwards and now has a zone length and position comparable with those in Figure 2. In fact, the parameters T_p, a_U and a_L are chosen purposely to provide a best fit to the experimental results.

Because of the lens effect of the molten zone (the refractive index of $NaNO_3$ is about 1.46[36]), both the visualized flow patterns and melt/solid interface shapes in Figure 2 have been optically distorted. In order to perform a further comparison, the calculated streamlines and interfaces are transformed to the optically distorted domain as shown on the RHS of Figure 15. A detailed description of this transformation is given elsewhere.[40] In Figure 15 the LHS of Figure 2 has also been included together with the calculated streamlines and interface shapes for comparison.

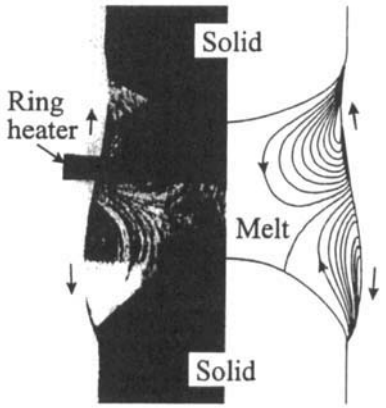

Figure 15. Comparison of the calculated results with Figure 2. The LHS shows the experimental photograph of flow patterns and interface shapes for a 2 mm radius $NaNO_3$ floating molten zone[23] and the RHS the optically transformed results from Figure 14(c)

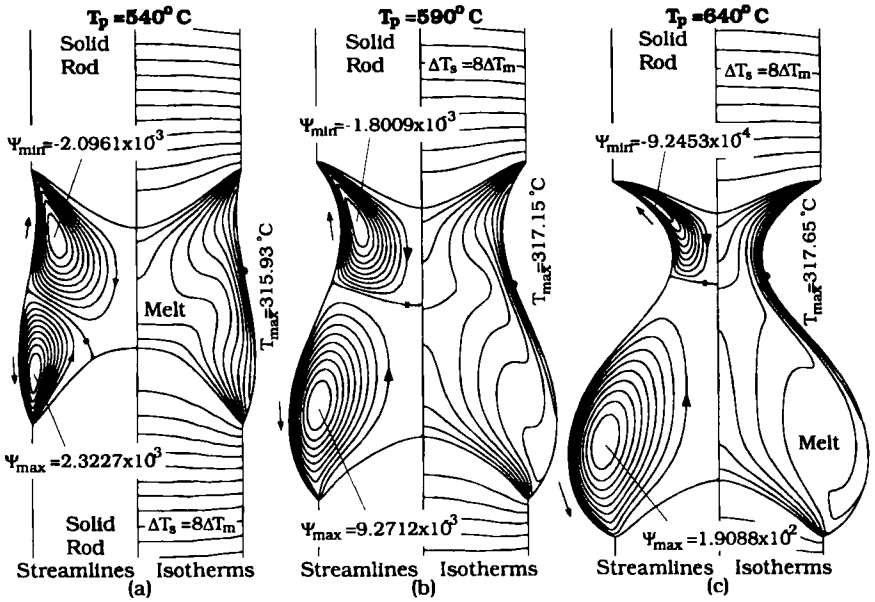

Figure 16. Effect of T_p: (a) T_p = 540 °C; (b) T_p = 590 °C; (c) T_p = 640 °C

Interestingly, not only the flow loops and zero streamline but also the melt/solid interfaces and the free surface shape of the calculated results are in good agreement with the observed ones.

5.4. Effects of heat input

As mentioned previously, an asymmetrical convection loop can affect the zone position. In order to show this effect, it is necessary to increase the zone length to produce a larger surface deformation; the zone length can in turn be adjusted by T_p. Meanwhile, a symmetrical T_a ($a_U = a_L = 0.3$ cm) is adopted again for the calculation. The effect of T_p is illustrated in Figure 16,

in which T_p ranges from 540 to 640°C. As shown in Figure 16(a), at $T_p = 540$°C the intensities of the two loops are comparable. Although the lower part of the zone has a little more space for convection, the upper loop has two driving forces, since both thermocapillary flow and natural convection are in the same direction. When T_p is increased to 590°C, as shown in Figure 15(b), the lower part of the molten zone bulges significantly while the upper part necks inwards. The intensity of the lower convection loop is increased from $2{\cdot}3227 \times 10^{-3}$ to $9{\cdot}2712 \times 10^{-3}$ g s^{-1}, while the upper one is decreased to $1{\cdot}8009 \times 10^{-3}$ g s^{-1}. Clearly, owing to the significantly stronger convection and higher T_p, the zone length beneath the heater increases significantly, while the upper one increases only slightly. A further increase in T_p makes this effect even more pronounced, as shown in Figure 16(c). At this point, owing to the extreme necking of the zone, the zone length (6·76 mm) almost reaches its stability limit. When T_p is increased even further, no convergent result can be obtained; presumably the molten zone no longer holds. It has to be pointed out that the stronger convection is not the only factor that causes a longer zone length in the lower part of the zone. The heat flux to the molten zone is also affected by the zone shape; the bulging surface may receive more heat than the necked one owing to its larger surface area and shorter distance to the heater. In fact, it has been observed experimentally[23] that at such a zone length the lower part of the zone could be more than two times longer than the upper one.

6. CONCLUSIONS

(1) A computer model based on the BFCFVM/Newton scheme is used to study the steady heat transfer, fluid flow and interfaces in a floating molten zone. Both natural convection and thermocapillary flow are considered and the free surface and melt/solid interfaces are calculated simultaneously.
(2) During Newton iteration the Jacobian matrix is estimated efficiently by finite differences, while the linear Newton equations are solved by the ILU(0) preconditioned GMRES iterative matrix solver. This approach has proven to be effective and has achieved nearly quadratic convergence.
(3) Natural convection encourages heat transfer towards the upper melt/solid interface and thus shifts the molten zone upwards. The melt/solid interface are very flat when natural convection is dominant in the melt zone.
(4) For a 2 mm radius $NaNO_3$ floating molten zone, thermocapillary convection is dominant in the melt. As compared with the case of no convection, the melt zone is lengthened at the free surface but shortened at the centreline, resulting in very convex melt/solid interfaces. The calculated flow patterns and interface shapes are also compared with those observed in experiments and are found to be in good agreement.
(5) Owing to gravity, the lower part of the zone bulges outwards, while the upper one necks inwards. In the bulging part the thermocapillary convection is stronger and melts back the (lower) melt/solid interface more as compared with the necked (upper) one. The effect becomes even more pronounced when the zone length gets longer. This is also consistent with the experiments.

ACKNOWLEDGEMENT

This work is supported by the National Research Council of the Republic of China under Grant NSC82-0402-E008-170.

REFERENCES

1. C. Chang and W. R. Wilcox, 'Inhomogeneities due to thermocapillary flow in floating zone melting', *J. Cryst. Growth*, **28**, 8–12 (1975).
2. P. A. Clark and W. R. Wilcox, 'Influence of gravity on thermocapillary convection in floating zone melting of silicon', *J. Cryst. Growth*, **50**, 461–469 (1980).
3. N. Kobayashi, 'Computer simulation of the steady flow in a cylindrical float zone under low gravity', *J. Cryst. Growth*, **66**, 63–72 (1984).
4. W. W. Fowlis and G. O. Roberts, 'Confinement of thermocapillary floating zone flow', *J. Cryst. Growth*, **74**, 301–320 (1986).
5. A. Rybicki and J. M. Floryan, 'Thermocapillary effects in liquid bridges', *Phys. Fluids*, **30**, 1956–1972 (1987).
6. R. Natarajan, 'Thermocapillary flows in a rotating float zone under microgravity', *AIChE J.*, **35**, 614–624 (1989).
7. Y. Zhang and J. I. D. Alexander, 'Surface tension and buoyancy-driven flow in a non-isothermal liquid bridge', *Int. j. numer. methods fluids*, **14**, 197–215 (1992).
8. J. R. Hyer, D. F. Jankowski and G. P. Neitzel, 'Thermocapillary convection in a model float zone', *AIAA J. Thermophys. Heat Transfer*, **5**, 577–582 (1991).
9. C. W. Lan, 'Computer simulation of heat transfer, fluid flow, and interfaces in a floating molten zone: a half-zone configuration', *Int. J. Heat Mass Transfer*, submitted.
10. J. L. Duranceau and R. A. Brown, 'Finite element analysis of melt convection and interface morphology in earthbound and microgravity floating zones', *AIP Conf. Proc.*, **197**, 133–144 (1989).
11. C. W. Lan and S. Kou, 'Heat transfer, fluid flow, and interface shapes in floating-zone crystal growth', *J. Cryst. Growth*, **108**, 351–366 (1991).
12. C. W. Lan and S. Kou, 'Effect of rotation on heat transfer, fluid flow, and interfaces in normal gravity floating-zone crystal growth', *J. Cryst. Growth*, **114**, 517–535 (1991).
13. C. W. Lan and S. Kou, 'Radial dopant segregation in zero-gravity floating-zone crystal growth', *J. Cryst. Growth*, **132**, 578–591 (1993).
14. C. W. Lan and S. Kou, 'Effect of rotation on radial dopant segregation in microgravity floating-zone crystal growth', *J. Cryst. Growth*, **133**, 309–321 (1993).
15. T. Surek and R. Coriell, 'Shape stability in float zoning of silicon crystals', *J. Cryst. Growth*, **37**, 253–271 (1977).
16. S. R. Coriell and M. R. Cordes, 'Theory of molten zone shape and stability', *J. Cryst. Growth*, **42**, 466–472 (1977).
17. H. M. Ettouney and R. A. Brown, 'Finite-element methods for steady solidification problems', *J. Comput. Phys.*, **49**, 118–150 (1983).
18. S. F. Kistler and L. E. Scriven, 'Coating flow theory by finite element and asymptotic analysis of the Navier–Stokes system', *Int. j. numer. methods fluids*, **4**, 207–229 (1984).
19. P. Hood, 'Frontal solution program for unsymmetric matrices', *Int. j. numer. methods eng.*, **10**, 397–399 (1976).
20. D. S. Dandy and L. G. Leal, 'A Newton's method scheme for solving free-surface flow problems', *Int. j. numer. methods fluids*, **9**, 1469–1486 (1989).
21. I. S. Duff, 'MA32—a package for solving sparse unsymmetric systems using the frontal method', *Rep. AERE R10079*, HMSO, London 1983.
22. C. H. Bishof, A. Carle, G. Corliss, A. Griewank and P. Hovland, 'ADIFOR—generating derivative code from Fortran programs', *ADIFOR Working Note # 1, MCS-P2630991*, Mathematics and Computer Division, Argonne National Laboratory, 1991.
23. C. W. Lan and S. Kou, 'Flow visualization of a floating molten zone', in preparation.
24. C. W. Lan and S. Kou, 'Heat transfer and fluid flow in floating-zone crystal growth with a mostly covered melt surface', *Int. J. Heat Mass Transfer*, **35**, 433–442 (1992).
25. C. W. Lan and S. Kou, 'Thermocapillary and natural convection in a melt column with an unknown melt/solid interface', *Int. j. numer. methods fluids*, **12**, 59–80 (1991).
26. A. D. Gosman, W. M. Pan, A. K. Runchal, D. B. Spalding and M. Wolfshtein, *Heat and Mass Transfer in Recirculating Flows*, Academic, London, 1969.
27. M. Vinokur, 'An analysis of finite-difference and finite-volume formulation of conservation laws', *J. Comput. Phys.*, **81**, 1–52 (1989).
28. A. R. Curtis, M. J. D. Powell and J. K. Reid, 'On the estimation of sparse Jacobian matrices', *J. Inst. Math. Appl.*, **13**, 117–120 (1974).
29. T. F. Coleman, B. S. Garbow and J. J. More, 'Software for estimating sparse Jacobian matrices', *ACM Trans. Math. Softw.*, **10**, 329–347 (1984).
30. I. S. Duff, A. M. Erisman and J. K. Reid, *Direct Methods for Sparse Matrices*, Clarendon, Oxford, 1986.
31. I. S. Duff, 'MA28—a set of Fortran subroutines for sparse unsymmetric linear equations', *Rep. AERE R8730*, HMSO, London, 1977.
32. Y. Saad and M. H. Schultz, 'GMRES: a generalized minimal residual algorithm for solving nonsymmetric linear systems', *SIAM J. Sci. Stat. Comput.*, **7**, 856–869 (1986).
33. P. Sonneveld, 'CGS (conjugate gradients squared), a fast Lanczos-type solver for non-symmetric linear system', *Delft University of Technology, Rep. Department of Mathematics and Informatics No. 84-16*, 1984.
34. J. A. Meijerink and H. A. van der Vorst, 'An iterative solution method for linear systems of which the coefficient matrix is a symmetric M-matrix', *Math. Comput.*, **31**, 148–162 (1977).

35. J. H. Ferziger, 'A note on numerical accuracy', *Int. j. numer. methods fluids*, **8**, 995–996 (1988).
36. F. Preisser, D. Schwabe and A. Scharmann, 'Steady and oscillatory thermocapillary convection in liquid columns with free cylindrical surface', *J. Fluid Mech.*, **126**, 545–567 (1983).
37. W. J. Silliman and L. E. Scriven, 'Separating flow near a static contact line: slip at a wall and shape of a free surface', *J. Comput. Phys.*, **34**, 287–313 (1980).
38. D. Schwabe, A. Scharmann, F. Preisser and R. Oeder, 'Experiments on surface tension driven flow in floating zone melting', *J. Cryst. Growth*, **43**, 305–312 (1978).
39. C. W. Lan and S. Kou, 'Shortened floating-zone crystal growth under normal gravity', *J. Cryst. Growth*, **119**, 281–291 (1992).
40. C. W. Lan and S. Kou, 'Formulation for correcting optical distortions due to a transparent floating zone', *J. Cryst. Growth*, **132**, 471–476 (1993).